Chemical and Physical Aspects of the Misfit Layer Oxides $Tl_\alpha[(Sr_{1-y}Ca_y)O]_{1+x}(CoO_2)$

Ph. Boullay, R. Seshadri,† F. Studer, M. Hervieu,* D. Groult, and B. Raveau

Laboratoire CRISMAT, ISMRA et Université de Caen, Bd Marechal Juin, 14050 Caen Cedex, France

Received April 17, 1997. Revised Manuscript Received September 19, 1997⊗

Using a combination of microscopy, powder X-ray diffraction, and model building, we recently reported evidence for the first misfit layer oxide, $Tl_{0.41}(Sr_{0.9}O)_{1.12}CoO_2$ (Boullay *et al. Chem. Mater.* **1996**, *8,* 1482). In this work, we present a more detailed structural characterization from an additional high-resolution electron microscopy (HREM) study as well as extended X-ray absorption fine structures (EXAFS) from the Co K edge and the Tl L_{III} edge. We find a structural picture largely consistent with the one originally proposed, but much more quantitative. The work has been extended over a structural *family*, obtained by replacing Sr by Ca to obtain the title misfit phases. The evolution of composition and lattice parameters, as well as the magnetic and electrical transport properties of representative members of the misfit oxide family, are studied.

Introduction

In the so-called misfit layer compounds chemically distinct layered subsystems (usually two) are stacked alternately in a direction normal or nearly normal to the layers. While the stacking is crystallographic in the sense of being commensurate, the two subsystems can possess periods within the layers that are incommensurate with each other. Structures of this kind are found in some natural materials such as valleriite and cylindrite,[1] but numerous synthetic chalcogenides also adopt this kind of structure.[2] These misfit chalcogenides can be expressed by the general chemical formula $(MX)_{1+x}(TX_2)_m$ with $m = 1, 2, 3$ where M is Pb, Bi, Sn or a rare-earth; T is a transition element such as Ti, V, Cr, Nb, or Ta and X is S or Se. The term $(1 + x)$ reflects the incommensurate character and the nonstoichiometry usually associated with these compounds and is in the range $0.08 < x < 0.28$.

Recently, we reported the first misfit layer oxide[3] with the composition $Tl_{0.41}(Sr_{0.9}O)_{1.12}CoO_2$. This compound was clearly identified as a single-phase material that could be synthesized reproducibly and is distinct from all other compounds reported for the system Tl−Sr−Co−O. This compound presents two layered subsystems having mismatched periods along one direction of the layer plane. While certain experimental factors, including the inability to grow single crystals of the phase, its highly lamellar nature, and the limited diffraction data, prevented complete crystallographic analysis, a link was drawn with the sulfide $(PbS)_{1.18}(TiS_2)$[4] so that a structural model could be proposed. The subsystem S_1 ($a \simeq 4.95$ Å, $b_1 \simeq 5.02$ Å, $c \simeq 11.66$ Å, $\beta \simeq 97.7°$) describes strontium deficient rock salt layers $[(Sr_{0.9}\square_{0.1})O]_\infty$, whereas the subsystem S_2 ($a \simeq 4.95$ Å, $b_2 \simeq 2.81$ Å, $c \simeq 11.66$ Å, $\beta \simeq 97.7°$) corresponds to the $[CoO_2]_\infty$ slice comprising CoO_6 octahedra with a CdI_2 structure. The thallium atoms in the model are located between the two kinds of layers in a distorted tetrahedral coordination. Their presence would ensure the cohesion of the structure. The structure is depicted schematically in Figure 1.

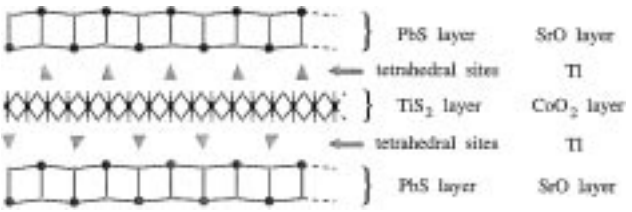

Figure 1. Schematic drawing of the proposed model for the misfit layer oxides structure in relationship with the misfit layer sulfides.

In this study, we present further investigations on these misfit phases, including evidence for a whole family of oxides when Sr is replaced by Ca. The electrical transport and magnetic properties of some of these phases are presented as are investigations of the valence state and coordination of Co and Tl as inferred from X-ray absorption spectroscopy. For determining the local structure around Tl, such studies are invaluable since, in our structural model, the Tl atoms stuff voids in a manner that might not necessarily result in a crystalline Tl network. The importance of these studies is 2-fold. The first is that they extend over a family, the structural postulates made in ref 3. The

† Presently at Institut für Anorganische Chemie und Analytische Chemie, Johannes Gutenberg Universität, Becherweg 24, Mainz D55099, Germany

⊗ Abstract published in *Advance ACS Abstracts,* November 15, 1997.

(1) Makovicky, E.; Hyde, B. G. *Struct. Bonding* **1981**, *46,* 101.
(2) Rouxel, J. *C. R. Acad. Sci. (Paris)* **1996**, *II-b 323,* 41.
(3) Boullay, Ph.; Domenges, B.; Hervieu, M.; Groult, D.; Raveau, B. *Chem. Mater.* **1996**, *8,* 1482.
(4) Van Smaalen, S.; Meetsma, A.; Wiegers, G. A.; De Boer J. L. *Acta Crystallogr.* **1991**, *B47,* 314.

S0897-4756(97)00232-9 CCC: $15.00
Published on Web 01/19/1998

second is that, being a new class of oxide materials, their properties are of considerable interest.

Experimental Section

The compounds were synthesized in two steps: first a mixture of Co_3O_4, $SrCO_3$, and/or $CaCO_3$ were ground in an agate mortar and heated in air at 950 °C for 24 h, for decarbonation. Tl_2O_3 was then added in order to realize the nominal cationic composition $Tl_\alpha(Sr_{1-y}Ca_y)_nCo$. After being finely ground, the powders were packed in alumina fingers either directly or in the form of small pressed bars and sealed in evacuated silica tubes. The samples were heated at 880 °C for 20 h and slowly cooled to room temperature. The terms α, y, and n were modified and showed that the homogeneity range in this family is large. Syntheses are reproducible for specific α, y, and n values.

The samples for electron microscopy were crushed in 1-butanol in an agate mortar and deposited onto a holey carbon film. The electron diffraction (ED) study was carried out with a JEOL JEM 200CX electron microscope fitted with an eucentric goniometer (±60°). The high-resolution electron microscopy was performed with a TOPCON 002B microscope equipped with a ±10° double-tilt goniometer and an objective lens with a spherical aberration constant of 0.4 mm. Both microscopes are equipped with KEVEX EDS analyzers. HREM image simulations were carried out using the multislice method implemented in the MAC TEMPAS and NCEMSS programs.[5]

The X-ray powder diffraction (XRPD) patterns were registered on a Philips diffractometer (PW3710 based) equipped with a graphite backscattering monochromator and using Cu Kα radiation. The cell parameters were extracted from the data with the program FULLPROF in a profile-matching mode.[6]

Magnetic measurements were performed on a Quantum Design MPMS SQUID magnetometer on small bars of the samples. The susceptibility as a function of temperature was measured on heating from 5 to 300 K under a field of 3000G after field cooling (FC) and zero-field cooling (ZFC). The susceptibilities were corrected for the core diamagnetic contributions of each of the ions, but demagnetization corrections were not made. Electrical resistance as a function of temperature was studied on sintered bars of the sample using the four-probe technique. Copper leads were attached to the samples using silver paint or indium solder. Due to the samples being poorly sintered and rather fragile, the contacts could not be made in any precise geometry, so the measurement of dimensions proved to be difficult. As a result, only the scaled resistance of the samples are reported and not the specific resistivity.

The Co K and Tl L_{III} edges X-ray absorption spectra were recorded at room temperature in transmission mode at LURE (Orsay) using synchrotron radiation from the DCI storage ring operating at 1.85 GeV with a 250 mA current. The X-rays were monochromatized using a silicon (331) channel cut monochromator. The reference oxides, $LaCoO_3$ for Co K edge and Tl_2O_3 for Tl L_{III} edge, were systematically recorded before and after each studied sample in order to check for any energy shift. The normalization procedure used throughout this work was a standard one: after subtraction of the same linear background on the XANES and EXAFS spectra, recorded in the same experimental conditions, a point at high energy on the EXAFS spectra, where no more EXAFS oscillations were still observable, was set to unity. Then the intensity of another point with an energy between 50 and 100 eV from the edge was determined on the EXAFS spectrum and that was normalized to the intensity of the corresponding point in XANES spectrum.

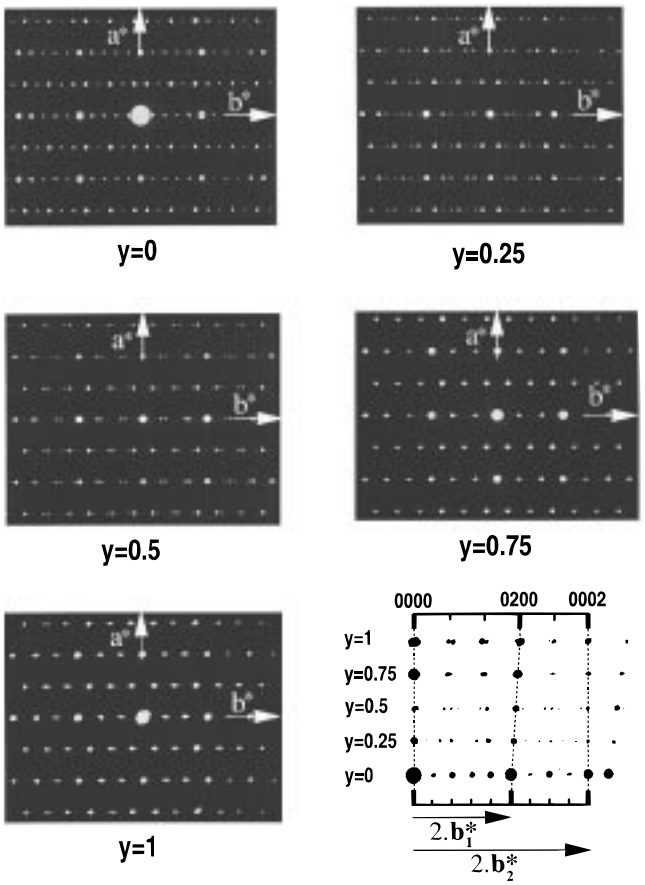

Figure 2. The evolution of the b_1/b_2 ratio vs y is seen from the [001] ED pattern (here for compounds with a nominal cationic composition $Tl(Sr_{1-y}Ca_y)Co$). The ratio regularly varies from 9/5 to 5/3 (for $y = 0$ to $y = 1$). For these starting compositions, we note the two subsystems are almost commensurate for $y = 0$ and $y = 0.75$.

The EXAFS data analysis was performed using the package written by Michalowicz.[7] The EXAFS contribution was extracted from the observed absorption $\mu(E)$ following conventional methods. The main atomic absorption beyond the edge $\mu_1(E)$ was fitted using a fifth-degree polynomial. The continuous sample absorption $\mu_0(E)$ was estimated by an analytical expression using the Lengeler−Eisenberg method.[8] The normalized EXAFS signal, with E_0 taken equal to the energy at half the edge jump, was then expressed as $\chi(\mathbf{k}) = [\mu(E) - \mu_1(E)]/[\mu_1(E) - \mu_0(E)]$ where $\mathbf{k}$ is the photoelectron wave vector. After applying a $\mathbf{k}^3$ weighting in order to compensate the signal attenuation for high $\mathbf{k}$ values, the EXAFS signal was Fourier transformed in the distance R space using a Kaiser window ($\tau = 2.5$). One obtains a radial distribution function around the absorbing atom where each peak, corresponding to one coordination shell, can be filtered and back Fourier transformed to the $\mathbf{k}$ space. The positions where peaks appear are lower than the real R distances due to the phase shifts induced in the photoelectron wave function by backscattering atoms. The theoretical backscattering phases and amplitudes were calculated using the McKale tables.

Within single scattering theory, the experimental data corresponding to each coordination shell can be fitted using the expression

(5) Kilaas, R. NCEMSS, National Center for Electron Microscopy, Materials Sciences Division, Lawrence Berkeley Laboratory, University of California, Berkeley CA 94720.

(6) Rodriguez-Carjaval, J. Proceedings of the Satellite Meeting on Powder Diffraction of the XVth Congress of Int. Union of Crystallography Toulouse, France, July 1990.

(7) Michalowicz, A. Logiciels pour la Chimie, Société Française de Chimie, Paris, **1991**, 102.

(8) Lengeler, B.; Eisenberg, P. *Phys. Rev.* **1980**, *B21*, 4507.

$$\mathbf{k}_i\chi(\mathbf{k}_i) = \sum_i \frac{N_i}{R_i^2} A_i(\mathbf{k}_i,R_i) \exp\left(-2\sigma_i^2\mathbf{k}_i^2 - \frac{2R_i}{\lambda(\mathbf{k}_i)}\right) \sin(2\mathbf{k}_i R_i + \phi_i(\mathbf{k}_i,R_i))$$

where N_i is the number of neighbors in the shell at distance R_i from the absorbing atom. $A_i(\mathbf{k}_i,R_i)$ and $\phi_i(\mathbf{k}_i,R_i)$ are respectively the amplitude and phase functions for this shell. σ_i is the Debye−Waller factor reflecting thermal and static disorder. $\lambda(\mathbf{k}_i)$ is the mean free path of the photoelectron.

Results

Substitution of Sr by Ca. The substitution of strontium by calcium was attempted partly in order to support the structural postulate of the previous study on $Tl_{0.41}(Sr_{0.9}O)_{1.12}CoO_2$. If Sr is associated only with the first subsystem S_1, only the parameters in this subsystem would be affected by the substitution. To follow the evolution of the cell parameters as a function of the substitution index y, X-ray powder and the electron diffraction were used. We have remarked in the previous study that only electron diffraction allows us to identify without ambiguity the misfit character of these materials. The value of the b_2 parameter and the mismatch between the b_1 and the b_2 parameters are clearly seen in the ED patterns with a [001] zone axis (Figure 2). The reconstitution of the reciprocal space, tilting about b^*, allows to determine the conditions limiting the reflection. For the fundamental reflections of each subsystem, the conditions are hkl: $h + k = 2n$ and for all the reflections the conditions are hk_1lk_2: $h + k_1 + k_2 = 2n$. This confirms that the centering translation ($^1/_2$, $^1/_2$, 0, $^1/_2$) and the R_4 Laue Class $C2/m(0,\beta,0)$ can be retained for the whole solid solution. Due to the lamellar character of the structure, the [010] and the [100] orientations are rarely observed. When observed, these orientations agree with the proposed cell parameters and especially the [100] ED patterns exhibit the two b_1 and b_2 parameters (Figure 3). The composition of the phases were simultaneously checked by EDS analyses. These results are reported in Table 1 for the different starting compositions.

On the Nonstoichiometry. The reliability between the starting and experimental (EDS) y values was satisfactory with the Sr:Ca:Co ratio being close to the nominal values. Thallium that was added in the second step of the synthesis process could not be controlled with the same precision, and the product showed a systematic deficiency of thallium, no matter what the starting amount used.

In the misfit layer chalcogenides $(MX)_{1+x}(TX_2)$, the term $(1 + x)$ is directly related to the ratio of the two mutually incommensurate b parameters by the formula:

$$(1 + x) = 2\frac{b_{(TX_2)}}{b_{(MX)}}$$

Depending on the nature of the M and T elements, only one composition is observed which is nonstoichiometric due to the mismatch of the two subsystems along the b direction (taking b to be the unique monoclinic axis). Additionally there can be a deficiency within each subsystem, and in particular, M deficiency in the sulfides is known.

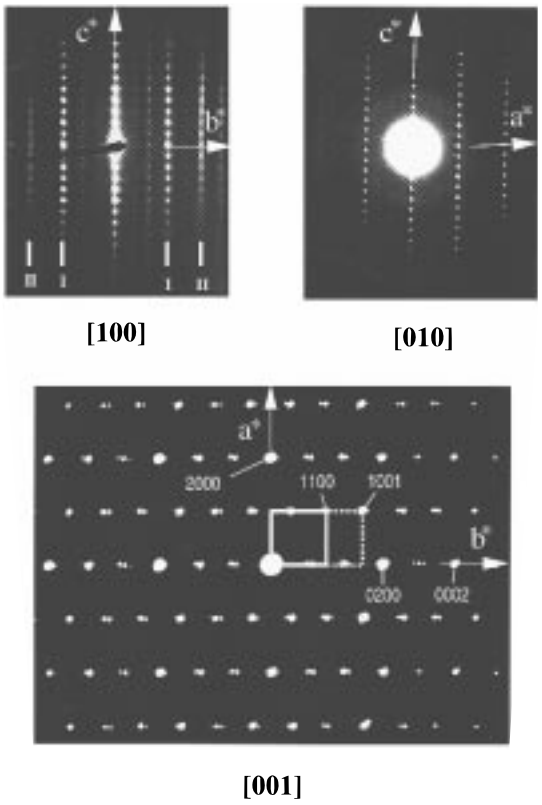

Figure 3. [100], [010], and [001] ED patterns for a $y = 1$ compound. On the [100] ED pattern, the rows of fundamental reflections are denoted by I for the first subsystem and by II for the second one. On the [001] ED pattern, the two subcells are outlined (white line for S_1 and dotted line for S_2). The indexation of the fundamental reflections of both subsystems is given in a quadridimensional formalism.

For the present misfit layer oxides, the mismatch between the subsystems also generates nonstoichiometry, and extra parameters might be necessary to take this in account. To this end we will use two extra parameters, α and n, and express the cationic composition as $Tl_\alpha(Sr_{1-y}Ca_y)_nCo$. In analogy with the chalcogenides the composition of the misfit layer oxides can then be expressed by the formula $Tl_\alpha[(Sr_{1-y}Ca_y)_{n/1+x}O]_{1+x}(CoO_2)$ where the rock-salt layers are alkaline-earth deficient. While some of the parameters (x, y, α, n) are interdependent, we do know precisely how they are so at the present time.

For these oxides, considering a fixed value of y ($0 \le y \le 1$), several nonstoichiometric compounds can be synthesized (with different α and n values). As a general trend one observes a decrease in α and in n when y increases. Slight modifications on the ratio of starting materials do not result in parasitic phases but are accommodated by the formation of misfit layer compounds having different compositions. Some of them are given in Table 1. As a result no "ideal" composition can be given for these compounds, and no simple link between the stoichiometry and the two mismatched b parameters seems to be possible.

Due to this nonstoichiometry, intrinsic to the misfit layer oxides, the compositions will be explicitly mentioned if needed, the specific phases will otherwise be referred to only by the y value.

Evolution of Lattice Parameters. The ED patterns (Figure 2) recorded for these compounds show that

Table 1. Nonstoichiometry in the Misfit Layered Oxides

cationic composition $Tl_\alpha (Sr_{1-y}Ca_y)_nCo$		chemical formulation
nominal	experimental (EDS) ±0.05	$Tl_\alpha[(Sr_{1-y}Ca_y)_{n/(1+x)}O]_{1+x}(CoO_2)$
$Tl_{0.5}Sr$	$Tl_{0.35}Sr_{0.95}$	$Tl_{0.35}[Sr_{0.85}O]_{1.12}(CoO_2)$
$Tl_{0.6}Sr$	$Tl_{0.41}Sr_{1.00}$	$Tl_{0.41}[Sr_{0.89}O]_{1.12}(CoO_2)$
$Tl_{0.5}Sr_{0.75}Ca_{0.25}$	$Tl_{0.33}(Sr_{0.74}Ca_{0.26})_{0.94}$	$Tl_{0.33}[(Sr_{0.74}Ca_{0.26})_{0.82}O]_{1.14}(CoO_2)$
$Tl_{0.5}Sr_{0.5}Ca_{0.5}$	$Tl_{0.30}(Sr_{0.50}Ca_{0.50})_{0.95}$	$Tl_{0.30}[(Sr_{0.50}Ca_{0.50})_{0.82}O]_{1.16}(CoO_2)$
$Tl_{0.6}Sr_{0.5}Ca_{0.5}$	$Tl_{0.34}(Sr_{0.50}Ca_{0.50})_{0.90}$	$Tl_{0.34}[(Sr_{0.50}Ca_{0.50})_{0.78}O]_{1.16}(CoO_2)$
$Tl_{0.5}Sr_{0.25}Ca_{0.75}$	$Tl_{0.23}(Sr_{0.25}Ca_{0.75})_{0.91}$	$Tl_{0.23}[(Sr_{0.25}Ca_{0.75})_{0.77}O]_{1.18}(CaO_2)$
$Tl_{0.5}Ca$	$Tl_{0.17}Ca_{0.89}$	$Tl_{0.17}[Ca_{0.74}O]_{1.20}(CoO_2)$
$Tl_{0.6}Ca$	$Tl_{0.25}Ca_{0.88}$	$Tl_{0.25}[Ca_{0.73}O]_{1.20}(CoO_2)$

Table 2. Lattice Parameter Evolution

Cationic Composition $Tl_\alpha (Sr_{1-y}Ca_y)_nCo$

y	α	n	a (Å)	b_1 (Å)	c (Å)	b_2 (Å)	β	$b_1/b_2 \sim$ m/p	% strain
0[a]	0.41	1.00	4.95	5.022	11.66	2.807	97.76	1.789 ~ 9/5	0.6
0	0.35	0.95	4.95	5.04	11.59	2.80	97.84	1.8 = 9/5	0
0.25	0.33	0.94	4.92	4.92	11.48	2.80	97.79	1.757 ~ 7/4	0.4
0.5	0.30	0.95	4.89	4.83	11.38	2.80	97.87	1.725 ~ 7/4	1.4
0.75	0.23	0.91	4.86	4.73	11.24	2.80	97.95	1.689 ~ 5/3	1.3
1.0	0.17	0.89	4.82	4.60	11.05	2.80	98.05	1.643 ~ 5/3	1.4

[a] Reference compound in ref 3.

the b_2 parameter is unaffected by the substitution of Sr by Ca. The evolution of the lattice parameters (Table 2) versus y emphasizes therefore the point that alkaline-earth elements are unique to the first subsystem. The substitution of Ca for Sr therefore affects only the parameters common to both subsystems (a, c and β and b_1). The decrease of the b_1 parameter is due to the difference in the cation size, the cubic cell parameters of SrO and CaO being 5.16 and 4.81 Å, respectively. The a parameter is common to both subsystems so the effect of substitution is less important for this parameter. The evolution of the c parameter would be governed firstly by the substitution of *Sr* by *Ca*. When y increases, the thickness of the AO (A =Sr, Ca) slice would decrease and thus so would c. Secondly for a given y value, the variation in the amount of thallium in the interlayer region would also affect the c parameter.

The ratio b_1/b_2 decreases monotonically with an increase in y. For $y = 0$ the ratio is 9/5, this changes to 7/4 for $y = 0.5$ and finally to 5/3 for $y = 1$. Considering the nearest commensurate supercell with a b_{CS} parameter equal to $pb_1 = mb_2$, the strain $((m/p - b_1/b_2)/(m/p))$ induced by the mismatch of these two periods varies with the nominal composition but always remains less than 2% (Table 2).

X-ray Absorption Spectroscopy

As mentioned in the previous report, the crystallographic information accessible for the second subsystem is meager. Whereas the ED patterns provide evidence for two distinct subsystems, only the first subsystem is observed in the X-ray powder diffraction patterns. Moreover, considering the complexity of the material, we were, up to now, not able to determine the structure from the observed X-ray diffraction patterns. In particular the location of thallium atoms inside the structure could be postulated but not verified.

To improve the quantitative aspect of the structural model, X-ray absorption spectroscopy was thought to be a useful tool. In particular, an accurate knowledge of the local environment around atoms can be obtained, allowing a coherent structural description. X-ray absorption spectra at the Tl L_{III} edge and Co K edge, including the extended X-ray absorption fine structures (EXAFS) were thus analyzed.

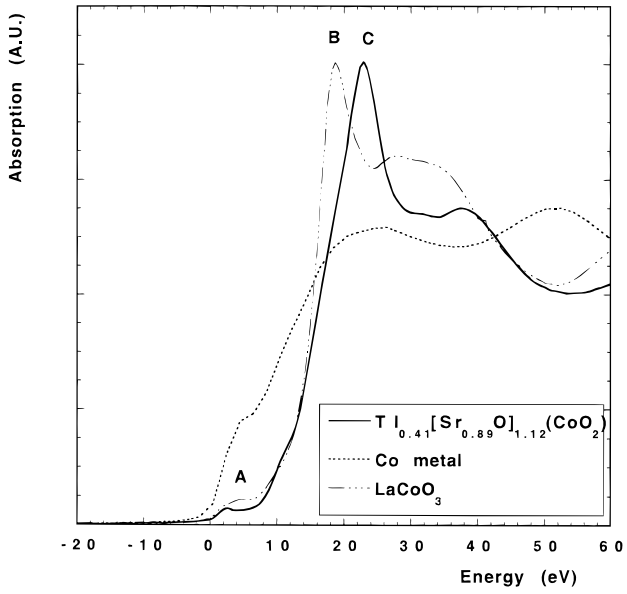

Figure 4. CoK X-ray absorption edge spectra for $y = 0$ and for the reference compounds.

The X-ray Absorption Edges. *The Cobalt K Edge.* The cobalt K edges for two reference compounds, Co metal and the perovskite $LaCoO_3$ for Co(III) valence state in a regular octahedron ($d_{Co-O} = 1.91$ Å), are shown in Figure 4. The Fermi level E_F ($E = 0$) was set to the first derivative peak of the metal edge.

The $LaCoO_3$ edge exhibits a narrow white line (B) characteristic of the single electronic transition 1s → 4p in a regular octahedral field. The small intensity of the prepeak (A), due to the transition from the 1s core level to the hybridized Co(3d) − O(2p) − Co(4s,4p) molecular levels, is also in agreement with a centrosymmetric environment of cobalt for which this hybridization is smaller than in distorted or noncentrosymmetric polyhedra (such as tetrahedra).

Unfortunately no pure Co(IV) oxide was available until recently, but the strontium ($y = 0$) misfit com-

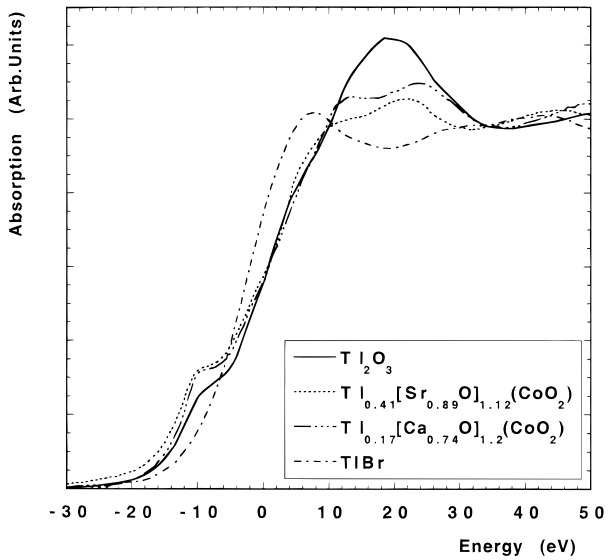

Figure 5. Tl L_{III} X-ray absorption edge spectra for $y = 0$ and $y = 1$ and for the reference compounds.

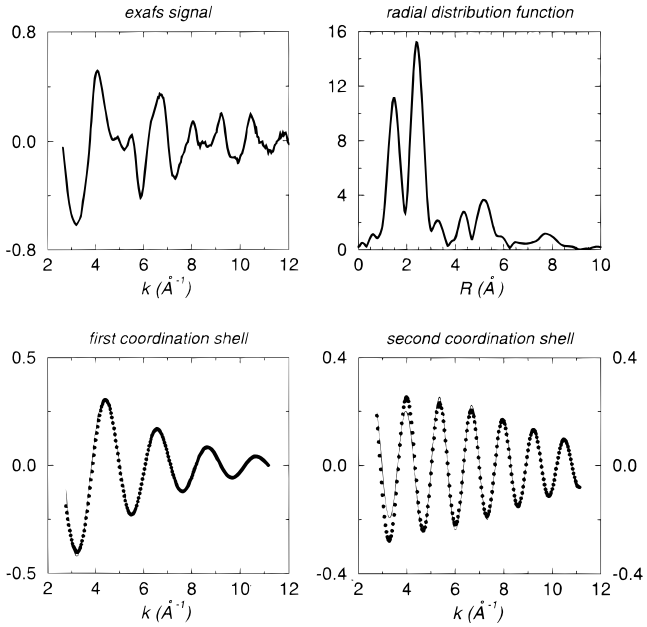

Figure 6. EXAFS at the Co K edge for a $y = 0$ compound. For the two simulations of the coordination shell, the experimental EXAFS signal are represented as continuous lines whereas the calculated ones are represented by dots.

pound edge shows clearly a shift toward higher energy with respect to the $LaCoO_3$ reference. Although wider than in the reference oxide, the white line is also the main feature of the spectrum. This result, combined with the small intensity of the prepeak, indicates a regular octahedral environment around cobalt. The width of the main line is very likely to result from the mixture of two lines due to the simultaneous presence of Co(III) and Co(IV) valence states.

The Thallium L_{III} Edge. The Tl L_{III} edges for two reference compounds, TlBr for Tl(I) and Tl_2O_3 for Tl(III), are shown in Figure 5 together with the strontium ($y = 0$) and calcium ($y = 1$) misfit compounds. Despite the large core hole width, an energy shift between the two reference compounds is clearly observed. On the contrary, no significant energy shift between the Tl_2O_3 edge and the misfit edges is observable within the energy reproducibility of this experiment (±0.3 eV), meaning that thallium is in the Tl^{III} valence state both in the Sr and the Ca compounds. The edges of the latter compounds show much better resolved features: both the prepeak A ($2p_{3/2} \rightarrow 5 - 6s$ transition) is more intense and the B ($2p_{3/2} \rightarrow 6d(t_{2g})$) and C peaks ($2p_{3/2} \rightarrow 6d(e_g)$) are better resolved than in Tl_2O_3.

These effects have been already observed in HTC thallium cuprates[9] and have been shown to be linked to a strongly distorted oxygen environment of thallium with two short (2.0 Å < d_{Tl-O} < 2.1 Å) and four long Tl−O distances (2.35 Å < d_{Tl-O} < 2.75 Å). In this case, the energy splitting of the e_g levels of the TlO_6 octahedra can be large enough to overlap with some t_{2g} levels, and thus the B transition on the spectra can disappear behind two C components due to $2p_{3/2} \rightarrow 6d_{x^2-y^2}$ and $2p_{3/2} \rightarrow 6d_{z^2}$ transitions. The above effects are also compatible with a tetrahedral environment of thallium as shown by neutron diffraction in single thallium layer cuprates.[10] In the latter case the B peak correspond to the $2p_{3/2} \rightarrow 6d(e_g)$ transition and the C peak to the $2p_{3/2} \rightarrow 6d(t_{2g})$ transition. Long Tl−O distances result in a negligible overlap between Tl(6d) and O(2p) orbitals, in no charge transfer from oxygen to thallium and thus in a strong prepeak. In conclusion, this edge study does not allow to distinguish these two possible environments. The main result is that the oxygen environment around thallium must present a strong distortion with two short and at least two long Tl−O distances.

EXAFS. *Cobalt Local Environment.* The experiment was recorded for a full strontium compound ($y = 0$), the EXAFS signal (Figure 6) between $\mathbf{k} = 2.6$ Å^{-1} and $\mathbf{k} = 11.5$ Å^{-1} was Fourier transformed in the R space in order to obtain the radial distribution function around the cobalt atoms (see modulus of the Fourier transform in Figure 6). Two significant coordination shells are observed and correspond to the mean distances of 1.45 and 2.40 Å before backscattering phase and amplitudes corrections. The ΔR ranges use for the back Fourier transform were $\Delta R = 0.9$ Å^{-1} and $\Delta R = 1$ Å^{-1}, respectively. EXAFS simulations were performed for these two first coordination shells, and the refined parameters are displayed in Table 3.

The fit of the filtered EXAFS spectra (Figure 6) corresponding to the first coordination shell exhibits a single peak and is well simulated with one Co−O distance. The local environment around the cobalt atoms corresponds then to an octahedron with six Co−O average distances equal to 1.92 Å, in agreement with the conclusion drawn from the edge study. The bond valence sums calculated with the program VALENCE[11] using the bond lengths from this EXAFS analysis indicate a +3.2 charge for the cobalt atoms, in agreement with the position of the absorption edge.

In our model, the cobalt atoms are closed packed in a layer at a distance of 2.83 Å corresponding to the b_2

(9) Studer, F.; Merrien, N.; Martin, C.; Michel, C.; Raveau, B.; Fontaine, A. *Physica* **1991**, *178*, 324.
(10) Michel, C.; Suard, E.; Caignaert, V.; Martin, C.; Maignan, A.; Hervieu, M.; Raveau, B. *Physica C* **1991**, *178*, 29.
(11) Hormillosa, C.; Healy, S., Computer code VALENCE, McMaster University, Hamilton, Ontario, Canada, 1991. Brown, I. D.; Altermatt, D. *Acta Crystallogr.* **1995**, *B41*, 244.

Table 3. Parameters for EXAFS Simulations

	species	N	R (±0.02 Å)	σ (Å)	residue	E_0 (±5 eV)	ind param[a]
			Composition $Tl_{0.41}[Sr_{0.89}O]_{1.12}(CoO_2)$				
Co K edge							
1st shell	O	6.00	1.92	4.6×10^{-2}	1×10^{-2}	7732	4
2nd shell	Co	6.00	2.83	5.7×10^{-2}	4.4×10^{-2}	7722	5
TL L_{III} edge							
1st shell	O	2.66	2.07	1×10^{-2}	9.1×10^{-3}	12670	5
	O	1.33	2.50				
2nd shell	Co	2.89	3.93	3.7×10^{-2}	3.3×10^{-2}	12666	6
	Sr	4.11	3.66				
	O	3.05	3.50	1.6×10^{-1}			
			Composition $Tl_{0.17}[Ca_{0.74}O]_{1.2}(CoO_2)$				
TL L_{III} edge							
1st shell	O	2.44	2.00	2×10^{-2}	1.3×10^{-2}	12664	4
	O	1.44	2.44				
2nd shell	Co	2.74	3.62	3.0×10^{-2}	3.1×10^{-2}	12662	4
	Ca	4.25	3.48				
	O	2.86	3.34				

[a] Number of independent parameters.

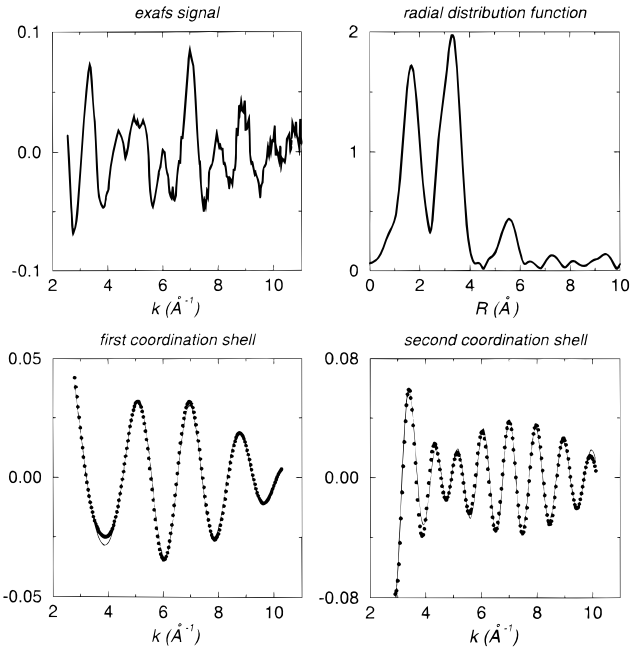

Figure 7. EXAFS at the Tl L_{III} edge for a $y = 0$ compound. For the two simulations of the coordination shell, the experimental EXAFS signal is represented as a continuous line whereas the calculated ones are represented by dots.

parameter and close to $a/\sqrt{3}$. The simulations were performed for the second coordination shell (Figure 6) with a scale factor close to the one use for the first coordination shell. The results confirm that the EXAFS oscillations mainly arise from Co−Co interactions and involve six cobalt neighbors at a mean distance of 2.83 Å.

From the study of the two first coordination shells surrounding the cobalt atoms, the structure of the second subsystem appears fully consistent with a CoO_2 layer having the CdI_2-type structure.

Thallium Local Environment. Two experiments were performed on the Tl L_{III} absorption edge, one record for a full strontium compound ($y = 0$) and one for a full calcium ($y = 1$) compound. The refined parameters used to fit the filtered EXAFS spectra are displayed in Table 3.

For $y = 0$ the EXAFS signal (Figure 7) between $\mathbf{k} = 2.8$ Å^{-1} and $\mathbf{k} = 10.4$ Å^{-1} was Fourier transformed in R space. In the radial distribution function (Figure 7) the first significant peak is located at the mean distance 1.68 Å whereas the second peak contain two distinct contributions one at 2.80 Å and the other at 3.35 Å before backscattering phase and amplitude corrections. The ΔR ranges used for the back Fourier transform were $\Delta R = 1.2$ Å^{-1} and $\Delta R = 1.4$ Å^{-1}, respectively for the first peak and for the two other peaks. The fit of the filtered EXAFS spectra corresponding to the first coordination shell (Figure 7) is achieved considering two kinds of distances, a short one at 2.07 Å and a long one at 2.50 Å, which is in agreement with the edge study. The number of neighbors is questionable, and these distances are the main result of the EXAFS analysis. Hence if the thallium atoms are located in distinct sites having similar Tl−O distances, the result would be an average number of neighbors involving all the different coordinations. In the previous paper the first coordination shell around the thallium atoms was supposed to correspond to a tetrahedral coordination. In this assumption one obtains an average number corresponding to 2.7 oxygens at 2.07 Å and 1.3 oxygens at 2.50 Å. This would suggest a distribution of thallium in tetrahedral environment consisting either of three short and one long (3 + 1) or two short and two long (2 + 2) Tl−O distances. Bond valence calculations assuming this tetrahedral oxygen coordination around Tl yields a bond valence sum of +2.6 in agreement with a Tl^{III} state.

For $y = 1$ the EXAFS signal (Figure 8) between $\mathbf{k} = 2.8$ Å^{-1} and $\mathbf{k} = 10.0$ Å^{-1} was Fourier transformed in R space. Two significant coordination shells are observed on the radial distribution function (Figure 8) and correspond to the mean distances 1.65 and 2.90 Å before backscattering phase and amplitude corrections. The ΔR ranges use for the back Fourier transform were $\Delta R = 1$ Å^{-1} and $\Delta R = 1.05$ Å^{-1}, respectively. For $y = 1$ the EXAFS study shows the first coordination shell around thallium atoms appear similar to the one observed for the $y = 0$ compound. The decrease of the Tl−O distances is consistent with both cell parameter evolution and with the edge study.

Assuming the Tl atoms are located between the CoO_2 and AO layers (A = Sr or Ca), there exist different tetrahedral sites which respect these two kind of distances. Two of the shortest Tl−O distances should mainly correspond to oxygen from the second subsystem

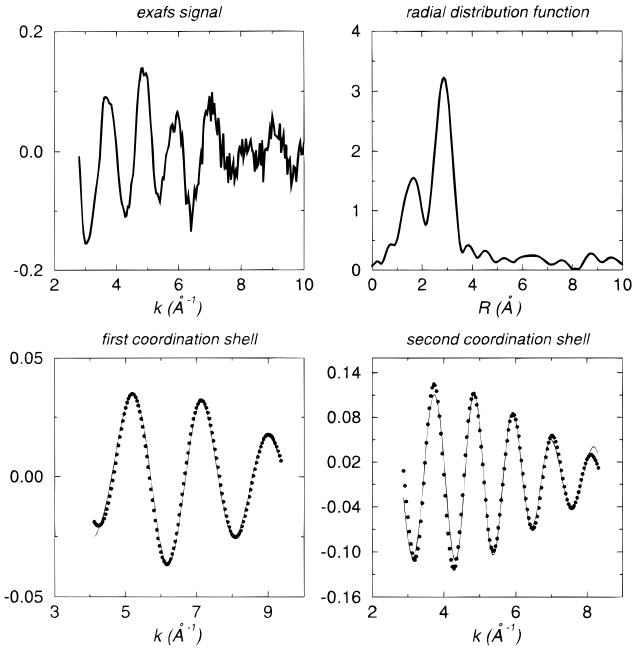

Figure 8. Analysis of the Tl L_{III} EXAFS spectra for a $y = 1$ compound. For the two simulations of the coordination shell, the experimental EXAFS signal is represented by continuous lines whereas the calculated ones are represented by dots.

whereas one of the long distances would correspond to a bond with one oxygen atom from the AO layer. In this case the longest perpendicular distance between the thallium and the oxygens of the AO layers can then be estimated close to 2.5 and 2.45 Å for $y = 0$ and $y = 1$, respectively. Now considering the deficient rock-salt layers, the Sr−O distances and the Ca−O distances would correspond respectively to 2.5 and 2.45 Å which is equal to the long distance found for the Tl−O bonds. Thus one cannot rule out the possibility of a partial occupation of the unoccupied alkaline earth sites of the AO layers by thallium atoms and especially for the calcium-substituted compounds as observed in materials such as in reference 12.

A study of the second coordination shell around thallium atoms was also attempted (Figure 7 for $y = 0$ and Figure 8 for $y = 1$). The EXAFS simulations (Table 3) performed on the basis of our structural hypothesis allow us to fit the main oscillations, but there are still some residual oscillations which probably arise from a truncation of the Fourier space. The strontium atoms from the first subsystem are located at about $2.5\sqrt{2} \simeq 3.54$ Å. This is in agreement with a perpendicular interlayer Tl−SrO distance about 2.5 Å and interatomic Sr−O distances about 2.5 Å inside the SrO slices. Again in the case where the thallium atoms are located in Sr sites inside the SrO slices the distance for Tl−Sr bonds would be equivalent. The above remarks are also true when Sr is replaced by Ca.

On the basis of both cobalt and thallium EXAFS analyses, rough atomic positions can be obtained for both subsystems which were used for the establishment of the HREM models in the next section.

(12) Goutenoire, F.; Caignaert, V.; Raveau, B. *J. Solid State Chem.* **1995**, *114*, 428.

HREM Study

One of the limit phases ($y = 1$) of the solid solution $Tl_{0.17}(Ca_{0.74}O)_{1.2}(CoO_2)$ was chosen to be characterized using high-resolution electron microscopy. Compared to the previous study made on a Sr-based compound,[3] the large difference between the scattering factor of thallium with respect to those of cobalt and calcium is favorable for determining the distribution of thallium atoms within the structure. In addition the presence of only one alkaline earth cation is expected to reduce the level of inhomogeneities.

Possible Structural Models. Since model-based image simulation is critical to the understanding of HREM images, we start with a structural model based on a commensurate supercell with parameters $a = 4.82$ Å, $b_s \sim 3b_1 \sim 5b_2 = 13.90$ Å, $c = 11.21$ Å, and $\beta = 97.8°$. Due to the low thallium content, namely ~0.2 per unit, and the Ca deficiency, two models for the location of Tl can be considered:

Model with Tl in the Rock Salt Layers. Tl can be located in 5-fold coordinated sites of the rock salt layer, occupying the Ca vacancies and resulting in the formation of one $[(Ca_{0.74}Tl_{0.12}O)_{1.2}]_\infty$ rock salt layer. This distribution could be statistical or ordered. This possibility was also be taken into consideration for the Sr misfit layer oxides but only as a marginal phenomenon. In fact the EXAFS study has already shown that the local environment for thallium appears quite similar for $y = 0$ and $y = 1$ compounds, and the existence of short Tl−O distances is hardly compatible with thallium atoms fully located within the CaO layers. We consider this possibility in analyzing the HREM images for the sake of completion.

Model with Tl Atoms Located between the Rock Salt and the Hexagonal Layers. Tl can occupy the tetrahedral sites, located between one $[(Ca,\square)]_\infty$ layer of the rock salt slice (subsystem S_1) and the oxygen layer $[O]_\infty$ of the $[CoO_2]_\infty$ hexagonal slice (subsystem S_2). The tetrahedra were assumed to be built from three oxygens in triangular arrangement in the hexagonal layer and one apical oxygen of the rock salt layer. In oxides, this second structural hypothesis seems to be favored by the ionic character of the bonds, contrary to the sulfides for which the covalent character of the structure allows a simple stacking of the two subsystems with van der Waals interactions. The problem would be then to determine the distribution of the thallium atoms in the resulting Tl layer. Due to the mismatch between the two subsystems, only a few positions are available for thallium in a tetrahedral environment as perfect as possible. In agreement with EXAFS results and considering the relative arrangement of the $[Ca_{0.74}O]_\infty$ and $[O]_\infty$ layers, two models can be used for HREM simulation purposes retaining a C-type lattice. The positional parameters were built with respect to the interatomic distances found from EXAFS analyses and the two models denoted as C2 and Cm are given in Table 4.

The crystallites were characterized by HREM selecting the [001] and [010] orientations. Images were calculated considering the above structural models, varying the focus values and the crystal thicknesses. For each of them, three different hypotheses of thallium content were considered: one without thallium, one

Table 4. Atomic Parameters for $Tl_{0.17}(Ca_{0.74}O)_{1.2}(CoO_2)$ HREM Simulations[a]

model C2 (SG: No 5)						model Cm (SG: No 8)					
element	*x*	*y*	*z*	site	occ	element	*x*	*y*	*z*	site	occ
Co1	0	0	0.5	2b	1	Co1	0	0	0.5	2a	1
Co2	0	0.2	0.5	2b	1	Co2	0	0.2	0.5	4b	1
Co3	0	0.4	0.5	2b	1	Co3	0	0.4	0.5	4b	1
Co4	0	0.6	0.5	2b	1	O1	0.31	0	0.413	2a	1
Co5	0	0.8	0.5	2b	1	O2	0.31	0.2	0.413	4b	1
O1	0.31	0	0.413	4c	1	O3	0.31	0.4	0.413	4b	1
O2	0.31	0.2	0.413	4c	1	O4	0.69	0	0.587	2a	1
O3	0.31	0.4	0.413	4c	1	O5	0.69	0.2	0.587	4b	1
O4	0.31	0.6	0.413	4c	1	O6	0.69	0.4	0.587	4b	1
O5	0.31	0.8	0.413	4c	1	Ca1	0.46	0	0.9	2a	0.74
Ca1	0.25	0	0.1	4c	0.74	Ca2	0.46	1/3	0.9	4b	0.74
Ca2	0.25	1/3	0.1	4c	0.74	Ca3	0.04	0	0.1	2a	0.74
Ca3	0.25	2/3	0.1	4c	0.74	Ca4	0.04	1/3	0.1	4b	0.74
O′1	0.75	0	0.1	4c	1	O′1	0.96	0	0.9	2a	1
O′2	0.75	1/3	0.1	4c	1	O′2	0.96	1/3	0.9	4b	1
O′3	0.75	2/3	0.1	4c	1	O′3	0.54	0	0.1	2a	1
						O′4	0.54	1/3	0.1	4b	1
Tl1	0.61	0	0.303	4c	0.42	Tl1	0.61	0	0.303	2a	0.28
						Tl2	0.39	0.2	0.697	4b	0.28

[a] Models in an ideal commensurate supercell $a = 4.82$ Å, $b = 13.90$ Å, $c = 11.21$ Å, and $\beta = 97.81°$.

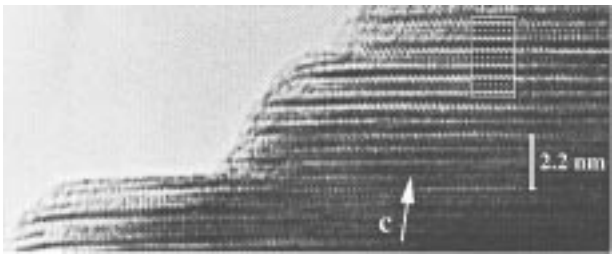

Figure 9. [010] HREM image: the modulation of the contrast in the level of the space between the $[(Ca, \square)O]_\infty$ double layer and the $[CoO_2]_\infty$ layer is interpreted by the presence of thallium atoms at this level. The theoretical contrast calculated from the C2 model is in good agreement with the experimental one.

with 0.2 Tl per unit (the experimental value), and one with a fully occupied thallium site.

[010] Orientation: Level of the Thallium Atoms. Figure 9 corresponds to an experimental image recorded for a focus value close to −250 Å for which the dark spots are correlated to the zones of high electron density. The major feature of this image is the presence of two bright rows. These bright rows are correlated to the space located between the $[Ca_{0.74}O]_\infty$ double layer and the $[CoO_2]_\infty$. For these bright rows, one observes a modulation of the contrast which can be correlated to the presence of thallium atoms at this level. Indeed the calculated images based on several structural models allow us to consider how the location of thallium can modify the contrast. In the thallium free model, as well as in a model were the thallium atoms are located inside the rock salt layer, the bright rows are continuous. From the simulations, the modulation of the contrast arises only when thallium atoms are distributed inside the interlayer space. The simulated image calculated for the C2 model is superimposed to the experimental image, showing a good fit (Figure 9).

Note that the overall images recorded along that direction or any other [*hk*0] show that the stacking mode of the different layers along the axis is regular, and no evidence of Ca vacancy ordering was detected.

[001] Orientation: Relative Disposition of the Thallium Layers. The projections of the thallium atoms along [001] are given in Figure 10 for the two

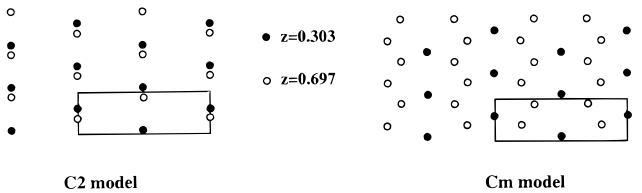

Figure 10. Projection of the thallium atoms along the [001] direction for the two models used for the HREM simulations.

models C2 and Cm. To describe the way the Tl are distributed in the tetrahedral sites of the $[Tl_{0.1}]_\infty$ layers, in each of the structural models, we can consider atomic rows parallel to $\vec{a}$ where the thallium are lined up. In the C2 model all the $[Tl_{0.1}]_\infty$ layers are built up only from single Tl rows, and the Tl positions of two adjacent Tl layers, sandwiching one $[CoO_2]_\infty$ slice, are projected onto two very close *xy* positions. In that way, the thallium distribution, projected along [001], appears as only single rows of thallium 7 Å spaced along *b* (Figure 10a). In the Cm model, there exist two types of Tl layers: one is built up from single Tl rows whereas the second one is built up from double *Tl* rows, and moreover, the double rows are shifted with regard to the single rows. As a result, single and double rows are differentiated in the projection along [001] (Figure 10b).

The two through focus series calculated for a thallium content corresponding to a total amount of thallium close to the experimental value, ∼0.2, are given in Figure 11b (model C2) and Figure 11c (model Cm) and are to be compared to that of the thallium free model Figure 11a. The key result obtained from such simulations is a verification of the presence of atoms stuffing the spaces between the two layers.

An experimental image recorded for a focus value where the cations positions are imaged as dark dots (close to −200 Å) is given in Figure 12. The most significant feature is the existence of prominent rows, running along $\vec{a}$, where bright and dark dots alternate, spaced 2.4 Å apart. In the major part of the crystals, these rows are single, spaced by 7 Å ($b_s/2$), and the bright dots are shifted by $a/2$ from one single row to the adjacent one. These single rows of bright dots are indicated by single large white marks in the figure. They

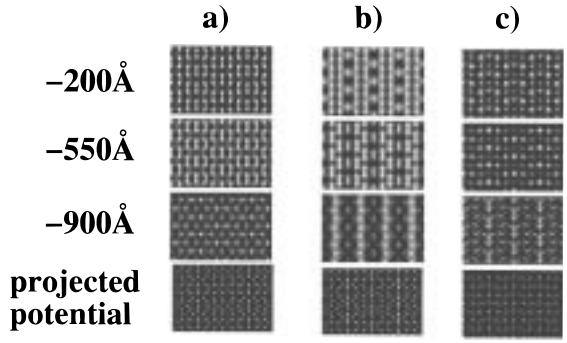

Figure 11. Theoretical [001] HREM images calculated (a) for a model without thallium, (b) for the C2 model, and (c) for the Cm model. Three representative focus values (−200, −550, and −900 Å) are represented and correspond to a crystal thickness of 22 Å.

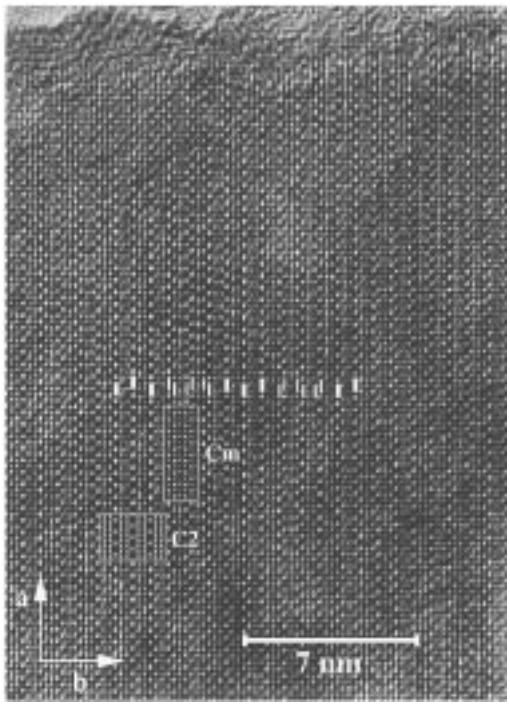

Figure 12. The existence of single (large white marks) and double (double white marks) rows of bright dots running along $\vec{a}$ is the signature of the thallium distribution. The theoretical images calculated for the commensurate supercells in the C2 and Cm space groups are superposed to the experimental one. They allow to interpret the existence of the single and double rows, respectively.

are separated by two rows of small gray dots. As shown by the calculated images (see for example Figure 11), these rows of intense spots are the signature of the presence of thallium. This contrast is usually established over a few unit cells, and then, another type of contrast is established over only one or two cells, where double rows of alternating bright spots are observed. The comparison with the calculated series shows that the first contrast is typical of the existence of only single Tl rows (i.e. model C2) whereas the second contrast is characteristic of a structure where double rows of alternating Tl exist, i.e. compatible with the Cm model. The double rows are indicated by double white marks in the Figure 12. The calculated images for a focus value close to −200 Å are superposed to the experimental image in Figure 12.

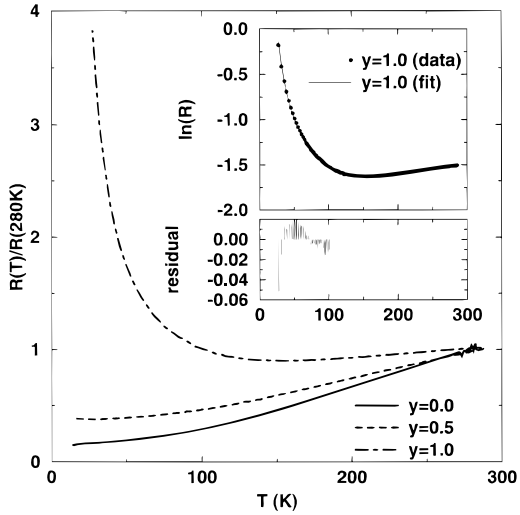

Figure 13. Electrical transport measurements. The temperature dependence of the scaled resistance $R(T)/R(280\ \mathrm{K})$ is plotted for samples corresponding to $y = 0$, $y = 0.5$, and $y = 1$.

The limitation of models built in an approximate commensurate supercell is then seen. Indeed we need a combination of the two models to describe the experimental images. In the C2 model as described above, single lines of bright dots are 7 Å apart and separated by two lines of gray dots. Locally, the separation of successive lines of bright dots is made by three lines of gray dots. This feature is always coupled with the variation of contrast which corresponds to the existence of a double row of alternating bright dots (Cm model).

The commensurate models cannot take into consideration special characteristics such as fact that the bright lines are shifted sideways by systematic ledging. Such a variation of the period was reported in the misfit layer sulfides[13] and explained in terms of periodic adjustment of the overlap pattern due to the fact that pb_1 is not strictly equal to mb_2. In the case of the present misfit layer oxides, where cations are needed between the two types of layers to ensure the cohesion, this phenomenon appears to be coupled with the presence of double thallium rows.

Theoretical images corresponding to a full occupancy of the thallium sites were calculated to take into consideration the possibility of coexistence of thallium rich and thallium poor areas. The corresponding contrast is so different from the experimental one that it allows us to discard definitively this hypothesis.

In conclusion, the HREM study shows that the structural mechanism proposed for the Sr-based misfit layer oxides can be retained for the solid solution and the calcium misfit layer oxide, $Tl_{0.17}(Ca_{0.74}O)_{1.2}(CoO_2)$. The structure can be described from the stacking, along [001], of two structures, one hexagonal (CoO_2) layer, and one rock salt type layer, bound together by $[Tl_{0.1}]$ slice, according to the sequence $[Tl_{0.1}]_\infty-[(Ca_{0.74}O)_{1.2}]_\infty-[Tl_{0.1}]_\infty-[CoO_2]_\infty$.

Physical Aspects

Electrical Transport. Figure 13 shows the temperature dependence of the scaled resistance $R(T)/R(280$

(13) Kuypert, A.; van Landuyt, J.; Amelinckx, S. *J. Solid State Chem.* **1990**, *86*, 212.

Table 5. Details of the Magnetic Study

sample y	composition	valence of Co	C	θ	χ_0 (10^{-4} emu mol^{-1})
0.0	$Tl_{0.35}[Sr_{0.85}O]_{1.12}CoO_2$	3.3	0.305(2)	−32.7(5)	1.63(4)
0.5	$Tl_{0.33}[(Ca_{0.5}Sr_{0.5})_{0.82}O]_{1.16}CoO_2$	3.4	0.300(2)	−22.1(6)	3.02(5)
1.0	$Tl_{0.17}[Ca_{0.74}O]_{1.20}CoO_2$	4.1	0.292(1)	−7.73)	2.92(4)

K) for samples corresponding to the nominal "cationic composition" $Tl_\alpha(Sr_{1-y}Ca_y)_nCo$ where $\alpha = 1$, $n = 1$ and where $y = 0$ (full Sr), $y = 0.5$ ($Ca_{0.5}Sr_{0.5}$), and $y = 1$(full Ca with $Tl_{0.17}$) (see Table 1). For these samples the resistivity at room temperature can be estimated to be in the range of 10^{-2}−10^{-3} Ω cm. The positive temperature coefficient of resistance (TCR) for the samples near and below the room temperature signifies that the misfit oxides exhibit metallic behavior. The $y = 0$ sample shows behavior typical of so called "dirty metals" with a TCR that is positive throughout but decreasing in magnitude as the temperature is decreased. This behavior corresponds to the dominant carrier-scattering mechanism at low temperature being due to impurities. In contrast, a "good" metal would display a resistivity that approached very small values rapidly (typically as $T^{3/2}$) as T approached 0 K.[14] . The tendency of the TCR to flatten out is more pronounced in the mixed $y = 0.5$ sample. When Sr is completely replaced by Ca, the behavior changes. The sample displays positive TCR at temperatures above ≃100 K but as the temperature is lowered, undergoes localization with the TCR becoming negative. However, the nature of the $R-T$ curve does not suggest a transition to an insulating state at least above 20 K. The low temperature data (below 100 K) of the $y = 1$ sample fits the expression for activated transport $\rho = \rho_0 \exp(E_{act}/RT)$ (inset of Figure 13). The fit can be described as satisfactory as seen from the residuals. From this fit, a small activation energy of ∼5 meV is obtained.

Magnetic Susceptibility. The determined formulae of the samples whose properties were studied, and the oxidation states of Co calculated from the formulae assuming Tl to be in the +3 oxidation state is given in Table 5. X-ray absorption edges unambiguously show that the thallium are in the Tl^{III} valence state. A valence state for *Co* larger than Co(III) is also in agreement with the conclusions drawn from the XAS. For each of the samples, the ZFC and FC data overlapped. Plots of $1/\chi$ vs T are shown in Figure 14 for the three samples, $y = 0$, 0.5, 1. Between 5 and 300 K there seems no clear indication of a magnetic transition. The data is poorly described by the Curie−Weiss law as clear from the temperature dependence. However, very satisfactory fits of the temperature dependence of the susceptibility of all three samples between 80 and 300 K could be obtained using the expression

$$\chi = \frac{C}{(T - \theta)} + \chi_0$$

which is the Curie−Weiss law with an additional term χ_0 that corresponds to a temperature independent contribution, possibly from free electrons. The values used to fit this expression to the data are presented in Table 5. The Curie parameter C is almost identical for

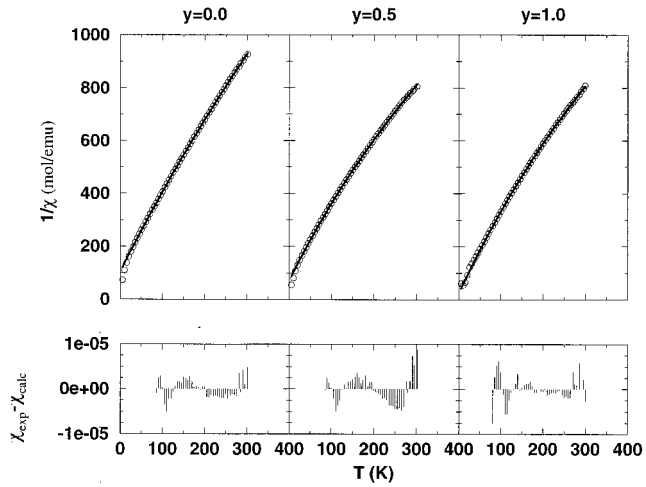

Figure 14. Magnetic susceptibility measurements. Plots of $1/\chi$ vs T for $y = 0$, 0.5, and 1 compounds.

all the samples, and the negative θ values indicate antiferromagnetic coupling between cobalt atoms. It must be mentioned that the lack of precision in the knowledge of the exact stoichiometry is expected to affect, to some degree, the values of the magnetic susceptibility through the value of the molar mass.

Discussion. The intrinsic mixed valence of cobalt in the misfit oxides is wholly consistent with the metallic temperature coefficient of resistivity seen at and below room temperature. The bronzes K_xCoO_2 with sheets of $CoO_2^{(4-x)+}$ arranged in the same manner as in the misfit oxides are metallic.[15] The Co−Co distance as obtained from the EXAFS study on the $y = 0.0$ phase (2.83 Å) are less than the critical distance of 2.87 Å suggested by Goodenough[16] for electrons in Co-based rock salt structures to be delocalized.[17] The proposed oxygen contents as shown in Table 5 are in agreement with high oxidation states of Co, and especially for $y = 1.0$, Co is found in the Co(IV) oxidation state. Using $\mu_{eff}^2/8 \simeq C \simeq n(n+2)/8$ where n is the number of unpaired electrons, we have for $C \simeq 0.3$ a value of $n \simeq 0.8$. If Co(III) $3d^6$ ($S = 0$) and Co(IV) $3d^5$ ($S = {}^1/_2$) are low spin, as expected for a rock salt contribution,[16] then this would correspond to a large proportion of Co(IV) in a very low distorted octahedral environment. It is worth noting that such a large amount of Co(IV) cannot be explained even by a full oxygen stoichiometry in the case of the *Sr* compound ($y = 0$). A mean oxidation state of 3.4 as shown in Table 5 could be accounted by the existence of some amount of intermediate spin ($S = 1$) or even high spin states ($S = 2$) of Co(III) as often observed in oxides.[18]

(14) Ashcroft, N. W.; Mermin, N. D. *Solid State Physics* W. B. Saunders: Philadelphia, PA, 1976.

(15) Delmas, C.; Fouassier, C.; Hagenmuller, P. *J. Solid State Chem.* **1975**, *13*, 165.

(16) Goodenough, J. B. In *Progress in Solid State Chemistry* Reiss, H., Ed.; Pergamon: New York, 1971; Vol. 5.

(17) While the CoO_2 layers belong within our model to the CdI_2 aristotype, the arrangement of octahedra within these layers permit the layers to be described as rock salt with the ⟨111⟩ direction in the layer.

In the case of the Ca compound ($y = 1$), oxygen nonstoichiometry can explain easily the amount of Co(IV) (80%) deduced from susceptibility measurements. But a reduction of this Co(IV) amount can be also obtained through the same mechanism of higher spin states for Co and may induce the same Co(IV) amount as in *Sr* compound. Thus a mean oxidation state of 3.3−3.5 can be reasonably proposed for Co in the samples studied. This results complement experiments such as chemical and XAS analyses.

These oxidation states and environment of Co are in agreement with the absorption edge and EXAFS analysis at least for the strontium compound as described in the XAS paragraph. The question why the $y = 1.0$ sample, with all the Sr replaced by Ca, shows localization must be addressed, particularly in light of the susceptibility behavior being more or less the same for all y. The nature of the gradual localization points to the role of disorder. In the present study, the quantity of Tl changes, as y changes. Likewise, the subsystem S_1 is compressed and the misfit strains change. All these factors can affect the transport behavior as discussed by Rouxel *et al.*[19] in the case of the misfit sulfides. The smaller quantity of Tl would result in more random local potentials where the Tl stuff the tetrahedral voids between the two sublattices. Such disorder is known to strongly affect transport in low dimensional materials.[20] At this stage, it would be premature to attempt a more detailed interpretation of the observed behavior.

CM9702326

(18) Barbey, L.; Nguyen, N.; Caignaert, V.; Studer, F.; Raveau, B. *J. Solid State Chem.* **1994**, *112*, 148.

(19) Rouxel, J.; Moëlo, Y.; Lafond, A.; DiSalvo, F. J.; Meerschaut, A.; Roesky, R. *Inorg. Chem.* **1994**, *33*, 3358.

(20) Lee, P. A.; Ramakrishnan, T. V. *Rev. Mod. Phys.* **1985**, *57*, 287.